

# The power spectrum of extended [C II] halos around high redshift galaxies

Meng Zhang<sup>1,2,3</sup>, Andrea Ferrara<sup>3★</sup>, Bin Yue<sup>1</sup>

<sup>1</sup>National Astronomical Observatories, Chinese Academy of Sciences, 20A, Datun Road, Chaoyang District, Beijing, 100101, China

<sup>2</sup>School of Astronomy and Space Science, University of Chinese Academy of Sciences, No.1 Yanqihu East Rd, Huairou District, Beijing 101408, China

<sup>3</sup>Scuola Normale Superiore, Piazza dei Cavalieri 7, 56126 Pisa, Italy

Accepted XXX. Received YYY; in original form ZZZ

## ABSTRACT

ALMA observations have detected extended ( $\approx 10$  kpc) [C II] halos around high-redshift ( $z \gtrsim 5$ ) star-forming galaxies. If such extended structures are common, they may have an impact on the line intensity mapping (LIM) signal. We compute the LIM power spectrum including both the central galaxy and the [C II] halo, and study the detectability of such signal in an ALMA LIM survey. We model the central galaxy and the [C II] halo brightness with a Sérsic+exponential profile. The model has two free parameters: the effective radius ratio  $f_{R_e}$ , and the central surface brightness ratio,  $f_\Sigma$ , between the two components. [C II] halos can significantly boost the LIM power spectrum signal. For example, for relatively compact [C II] halos ( $f_\Sigma = 0.4$ ,  $f_{R_e} = 2.0$ ), the signal is boosted by  $\approx 20$  times; for more extended and diffuse halos ( $f_\Sigma = 0.1$ ,  $f_{R_e} = 6.0$ ), the signal is boosted by  $\approx 100$  times. For the ALMA ASPECS survey (resolution  $\theta_{\text{beam}} = 1.13''$ , survey area  $\Omega_{\text{survey}} = 2.9 \text{ arcmin}^2$ ) the [C II] power spectrum is detectable only if the deL14d [C II] - SFR relation holds. However, with an optimized survey ( $\theta_{\text{beam}} = 0.232''$ ,  $\Omega_{\text{survey}} = 2.0 \text{ deg}^2$ ), the power spectrum is detectable for almost all the [C II] - SFR relations considered in this paper. Such a survey can constrain  $f_\Sigma$  ( $f_{R_e}$ ) with a relative uncertainty of 60% (20%). A successful LIM experiment will provide unique constraints on the nature, origin, and frequency of extended [C II] halos, and the [C II] - SFR relation at early times.

**Key words:** galaxies: formation—galaxies: high-redshift – dark ages, reionization, first stars – radio lines: galaxies

## 1 INTRODUCTION

Cosmic reionization, as the last major phase transition of the Universe, is a direct consequence of the formation of the first luminous objects. Determining the properties of galaxies in the Epoch of Reionization (EoR) is crucial to understand structure formation and evolution (Dayal & Ferrara 2018). However, our progress is hampered by the limited number of EoR sources that can be directly accessed via targeted observations. Such limitation is particularly severe for faint galaxies, which are thought to be the major sources of ionizing photons (Robertson et al. 2015; Mitra et al. 2015; Castellano et al. 2016) but are far below the detection limits of the current surveys (Salvaterra et al. 2013).

Line intensity mapping (LIM) is emerging as an efficient tool to detect these faint galaxies. LIM measures the integrated emission of spectral lines from all galaxies and the intergalactic medium (IGM) (see a review by Kovetz et al. 2017). By measuring fluctuations in the line emission from early galaxies, one could expect to obtain valuable physical insights about the properties of these sources and their role in reionization. Finally, LIM can be also used to put stringent constraints on cosmological models (Kovetz et al. 2019; Schaan & White 2021; Karkare et al. 2022).

There are several spectral lines of interest for intensity mapping including HI 21 cm line (Chang et al. 2010; Salvaterra et al. 2013), CO rotational lines (Breyse et al. 2014; Mashian et al. 2015; Li et al.

2016), bright optical emission lines such as Ly $\alpha$  and H $\alpha$  (Salvaterra et al. 2013; Pullen et al. 2014; Comaschi & Ferrara 2016; Gong et al. 2017; Silva et al. 2018) and the far-infrared (FIR) fine-structure lines (Gong et al. 2012; Uzgil et al. 2014; Silva et al. 2015; Yue et al. 2015; Serra et al. 2016; Yue & Ferrara 2019).

Among these, the [C II] emission line with wavelength  $157.7 \mu\text{m}$ , corresponding to the  $^2P_{3/2} \rightarrow ^2P_{1/2}$  forbidden transition of singly ionized carbon, is the brightest one in the FIR (Stacey et al. 1991), and a dominant coolant of the neutral ISM (Stacey et al. 1991; Wolfire et al. 2003) and dense photodissociation regions (PDR, Hollenbach & Tielens 1999). Therefore, the [C II] line can be used to probe the properties of the ISM at high redshift (Capak et al. 2015; Pentericci et al. 2016; Knudsen et al. 2016; Carniani et al. 2017; Bakx et al. 2020; Matthee et al. 2020).

Notably, a tight relation between [C II] luminosity and star formation rate (SFR) is found from both observations (De Looze et al. 2014; Herrera-Camus et al. 2015; Schaerer et al. 2020) and simulations (Vallini et al. 2015; Olsen et al. 2017; Leung et al. 2020). Therefore, the [C II] emission lines can be used to trace the star formation across cosmic time, albeit at high redshift the scatter around the local relation increases (Carniani et al. 2018). Conveniently, at early epochs, the line is shifted into the (sub-)mm wavelength range, which is accessible to ground-based telescopes such as the Atacama Large Millimeter/submillimeter Array (ALMA).

With the advent of ALMA, a large number of galaxies with [C II] emission line at  $z > 4$  have been detected, boosting the studies of the obscured star formation at high redshift (Hodge & da Cunha

★ E-mail: andrea.ferrara@sns.it

2020). Among these, a stacking analysis of ALMA observed galaxies (Fujimoto et al. 2019) discovered extended, 10 kpc scale [C II] halos around high redshift galaxies, whose size is  $\approx 5$  times larger than the UV size of the central galaxy. Similar results have been reported in the following studies both in subsequent stacking analysis (Ginolfi et al. 2020; Fudamoto et al. 2022) and individual galaxies (Fujimoto et al. 2020; Herrera-Camus et al. 2021; Akins et al. 2022; Lambert et al. 2022; Fudamoto et al. 2023).

The existence of extended [C II] halos around normal star-forming galaxies opens new perspectives for early metal enrichment. However, the physical origin of [C II] halos is still not clear. Possible scenarios include satellite galaxies, extended PDR or HII regions, cold streams, and outflows. These are discussed in Fujimoto et al. (2019). Indeed, the supernova-driven cooling outflow model explored by Pizzati et al. (2020, 2023) successfully produces the extended [C II] halo. This interpretation is also supported by Ginolfi et al. (2020), who found outflow signatures in the stacking analysis of [C II] emission detected by ALMA in 50 main sequence star-forming galaxies at  $4 < z < 6$ . Fujimoto et al. (2020) also suggested that the star-formation-driven outflow is the most likely origin of the [C II] halos. Finally, Herrera-Camus et al. (2021) found evidence of outflowing gas, which may be responsible for the production of extended [C II] halos. If [C II] halos are common in high redshift normal star-forming galaxies, they could leave a distinct imprint in LIM experiments.

In this paper, we aim to investigate the effects of extended [C II] halos on the LIM signal and their detectability. We first construct the [C II] halo model and compute the intensity mapping power spectrum of high redshift galaxy systems when both the central galaxy and extended [C II] halo are considered<sup>1</sup>. Then we analyze the detectability of the signal in ALMA intensity mapping survey and a proposed optimized survey. The paper is organized as follows: We outline our method in Section 2. Results, including the power spectrum signal and its signal-to-noise ratio estimation, are presented in Section 3. We finally summarize the results and give a discussion in Section 4.

## 2 METHOD

In the following, we describe our model to derive the LIM signal when both central galaxies and [C II] halos are considered. We start by constructing the extended [C II] halo model, and the relations between central galaxy [C II] luminosity, extended [C II] halo luminosity, and dark matter halo mass. We then compute the intensity mapping power spectrum, including one-halo and two-halo terms, and the shot noise term. Finally, we introduce the method to estimate the signal-to-noise ratio of the [C II] power spectrum, given the LIM survey parameters.

### 2.1 [C II] halo model

To compute the clustering term of the power spectrum, the first step is to model the [C II] radial surface brightness of the central galaxy and the extended halo. For this, we use a combined Sérsic+exponential model, where the central galaxy is described by the Sérsic model

(Sérsic 1963; Sérsic 1968) while the extended [C II] halo is described by the exponential function (Fujimoto et al. 2019; Akins et al. 2022).

The [C II] radial surface brightness of the central galaxy writes

$$\Sigma_{\text{CII,g}}(R) = C_g \exp \left[ -b_n \left( \frac{R}{R_{\text{e,g}}} \right)^{1/n} \right], \quad (1)$$

where  $C_g$  is the central surface brightness,  $R$  is the projected distance to the source center in the plane-of-sky,  $n$  is the Sérsic index, and  $R_{\text{e,g}}$  is the effective radius containing half of the integrated brightness. The term  $b_n$  is a function of  $n$ . It is obtained by solving the equation  $\Gamma(2n) = 2\gamma(2n, b_n)$ , where  $\Gamma(2n)$  is the Gamma function,  $\gamma(2n, b_n) = \int_0^{b_n} t^{2n-1} e^{-t} dt$  is the lower incomplete gamma function.

In the stacking analysis by Fujimoto et al. (2019), the central galaxies are well fitted by Sérsic model with  $n = 1.2$  and  $R_{\text{e,g}} = 1.1$  kpc. This is consistent with the rest-frame optical and UV sizes measured by Shibuya et al. (2015), who obtain a nearly constant value of  $R_{\text{e,g}}/R_{\text{vir}} = 1.0\% - 3.5\%$  for  $z = 0 - 8$ , where  $R_{\text{vir}}$  is the dark matter halo virial radius. Following these results, we adopt  $n = 1.2$  and fix  $R_{\text{e,g}} = 0.03R_{\text{vir}}$ .

For the extended [C II] halo, the surface brightness has the exponential form<sup>2</sup>

$$\Sigma_{\text{CII,h}}(R) = C_h \exp \left[ -b_1 \frac{R}{R_{\text{e,h}}} \right], \quad (2)$$

where  $b_1$  is the  $b_n$  for  $n = 1$ ,  $C_h$  is the surface brightness at the center and the  $R_{\text{e,h}}$  is the effective radius of the [C II] halo. We further assume  $C_h = f_\Sigma C_g$  and  $R_{\text{e,h}} = f_{R_e} R_{\text{e,g}}$ , where the ratios  $f_\Sigma$  and  $f_{R_e}$  are two free parameters in our work.

With the above surface brightness profiles, the [C II] luminosity for the central galaxy

$$\begin{aligned} L_{\text{CII,g}} &= \int 2\pi R \Sigma_{\text{CII,g}}(R) dR \\ &= 2\pi C_g \frac{n\Gamma(2n)}{(b_n)^{2n}} R_{\text{e,g}}^2, \end{aligned} \quad (3)$$

and for the extended [C II] halo

$$\begin{aligned} L_{\text{CII,h}} &= \int 2\pi R \Sigma_{\text{CII,h}}(R) dR \\ &= 2\pi C_h \frac{\Gamma(2)}{(b_1)^2} R_{\text{e,h}}^2. \end{aligned} \quad (4)$$

Since restricted by the sensitivity of the telescope in previous observations, the observed [C II] luminosity in deriving the [C II] - SFR relation is likely dominated by central galaxies. Moreover, as noted by Fujimoto et al. (2019), to fully capture the extended [C II] halos, additional mechanisms not involved in previous simulations are required. Therefore, we consider the previously-predicted [C II] - SFR relations (both by observations and by simulations) do not account for (or at least significantly underestimate) the extended [C II] halo contribution. For clarification, we shall use  $L_{\text{CII,SFR}} - \text{SFR}$  to denote the relations in the following of this work, where  $L_{\text{CII,SFR}}$  is the [C II] luminosity derived from the previously [C II] - SFR relations, see next subsection. We find the normalization by assigning  $L_{\text{CII,g}} \approx L_{\text{CII,SFR}}$ . Then

$$C_g = \frac{(b_n)^{2n}}{2\pi n \Gamma(2n) R_{\text{e,g}}^2} L_{\text{CII,SFR}}. \quad (5)$$

<sup>1</sup> Throughout the paper, we assume  $\Lambda\text{CDM}$  model with Planck Collaboration et al. (2016) cosmological parameters:  $\Omega_m = 0.308$ ,  $\Omega_\Lambda = 1 - \Omega_m = 0.692$ ,  $\Omega_b = 0.048$ ,  $h = 0.678$ ,  $\sigma_8 = 0.815$ ,  $n_s = 0.968$ .

<sup>2</sup> Note that the Sérsic model Eq. (1) is reduced to exponential function when  $n = 1$ .

Then the [C II] halo luminosity is also derived from the  $L_{\text{CII,SFR}}$  via

$$L_{\text{CII,h}} = f_{\Sigma} f_{R_e}^2 \frac{(b_n)^{2n}}{(b_1)^2} \frac{\Gamma(2)}{n\Gamma(2n)} L_{\text{CII,SFR}}, \quad (6)$$

and when  $n = 1.2$  it is reduced to

$$L_{\text{CII,h}} \approx 2.24 f_{\Sigma} f_{R_e}^2 L_{\text{CII,SFR}}. \quad (7)$$

We further assume that the profile is spherically symmetric, and perform a deprojection of the above surface density to obtain the 3D brightness profiles for the two components,  $\rho_{\text{CII,g}}(r)$  and  $\rho_{\text{CII,h}}(r)$ . This is given in Appendix A. The total 3D brightness profile is the sum of the two components

$$\rho_{\text{CII}}(r) = \rho_{\text{CII,g}}(r) + \rho_{\text{CII,h}}(r), \quad (8)$$

and we truncate it at  $R_{\text{vir}}$ . Then, the normalized Fourier transform of the profile in a dark matter halo of mass  $M_{\text{vir}}$ ,

$$u_{\text{CII}}(k|M_{\text{vir}}) = \frac{\int_0^{R_{\text{vir}}} dr 4\pi r^2 \frac{\sin kr}{kr} \rho_{\text{CII}}(r)}{\int_0^{R_{\text{vir}}} dr 4\pi r^2 \rho_{\text{CII}}(r)}, \quad (9)$$

which is used to compute the one-halo and two-halo terms of the power spectrum. The luminosity density profiles of the central galaxy and [C II] halo are shown in the left panel of Fig. 1. We take  $M_{\text{vir}} = 10^{12} M_{\odot}$  at  $z = 6$ ,  $f_{\Sigma} = 0.4$  and  $f_{R_e} = 6.0$ . In the right panel of Fig. 1 we show the Fourier transform of the profiles for different  $f_{R_e}$ .

## 2.2 The [C II] - dark matter halo mass relation

To derive the  $L_{\text{CII,SFR}} - M_{\text{vir}}$  relation, we first use the abundance matching method to get SFR –  $M_{\text{vir}}$  relation. Following Yue et al. (2015), we start from the observed (dust-attenuated) galaxy UV luminosity function (LF), which can be described by a Schechter function (Schechter 1976)

$$\frac{dn}{dM_{\text{UV}}^{\text{obs}}} = 0.4 \ln(10) \Phi^* 10^{-0.4(M_{\text{UV}}^{\text{obs}} - M_{\text{UV}}^*)} (\alpha + 1) \times \exp[-10^{-0.4(M_{\text{UV}}^{\text{obs}} - M_{\text{UV}}^*)}], \quad (10)$$

where the  $M_{\text{UV}}^{\text{obs}}$  is the dust-attenuated absolute UV magnitude, and the redshift-dependent parameters are taken from Bouwens et al. (2015),

$$\begin{aligned} M_{\text{UV}}^* &= -20.95 + 0.01(z - 6), \\ \Phi^* &= 0.47 \times 10^{-3-0.27(z-6)}, \\ \alpha &= -1.87 - 0.10(z - 6). \end{aligned} \quad (11)$$

Considering dust attenuation, the intrinsic absolute UV magnitude becomes

$$M_{\text{UV}} = M_{\text{UV}}^{\text{obs}} - A_{\text{UV}}, \quad (12)$$

where the UV dust attenuation is parametrized as

$$A_{\text{UV}} = C_1 + C_0 \beta \quad (A_{\text{UV}} \geq 0); \quad (13)$$

we set the coefficients  $C_0 = 2.10$  and  $C_1 = 4.85$ , following Koprowski et al. (2018). Finally, the UV spectral slope  $\beta$  is fitted by Bouwens et al. (2015)

$$\beta = \beta_0 + \frac{d\beta}{dM_0} (M_{\text{UV}}^{\text{obs}} - M_0), \quad (14)$$

with a redshift dependence given by

$$\begin{aligned} \beta_0 &= -1.97 - 0.06(z - 6), \\ \frac{d\beta}{dM_0} &= -0.18 - 0.03(z - 6). \end{aligned} \quad (15)$$

The intrinsic UV LF is related to the observed UV LF by

$$\frac{dn}{dM_{\text{UV}}} = \frac{dn}{dM_{\text{UV}}^{\text{obs}}} \frac{dM_{\text{UV}}^{\text{obs}}}{dM_{\text{UV}}}. \quad (16)$$

By assuming that the most massive galaxies occupy the most massive dark matter halos, we use the abundance matching method

$$\int_{M_{\text{UV}}} \frac{dn}{dM_{\text{UV}}} dM_{\text{UV}} = \int_{M_{\text{vir}}} \frac{dn}{dM_{\text{vir}}} dM_{\text{vir}}, \quad (17)$$

to derive the intrinsic absolute UV magnitude and dark matter halo mass relation. To get the SFR –  $M_{\text{vir}}$  relation, we assume that the intrinsic UV luminosity scales with the SFR (Kennicutt 1998)

$$\text{SFR} = K_{\text{UV}} L_{\text{UV}}, \quad (18)$$

where  $K_{\text{UV}} = 0.7 \times 10^{-28} M_{\odot} \text{ yr}^{-1} / (\text{erg s}^{-1} \text{ Hz}^{-1})$  (Bruzual & Charlot 2003) for a Chabrier (2003) stellar initial mass function (IMF), metallicity in the range  $0.005 - 0.4 Z_{\odot}$ , and stellar age  $> 100 \text{ Myr}$ ; we ignore the scatter on  $K_{\text{UV}}$  as discussed by Yue & Ferrara (2019).

The final step to get the  $L_{\text{CII,SFR}} - M_{\text{vir}}$  relation involves the  $L_{\text{CII,SFR}} - \text{SFR}$  relation. This can be parameterized as

$$\begin{aligned} \log L_{\text{CII,SFR}} &= \log \bar{L}_{\text{CII,SFR}} \pm \sigma_L \\ &= \log A + \gamma \log \text{SFR} \pm \sigma_L, \end{aligned} \quad (19)$$

where SFR is in units of  $M_{\odot} \text{ yr}^{-1}$ , and  $L_{\text{CII,SFR}}$  in units of  $L_{\odot}$ . We adopt six different  $L_{\text{CII,SFR}} - \text{SFR}$  relations to compute the power spectrum in our model. These relations are described in the following.

By combining a semi-analytical model of galaxy formation with the photoionisation code CLOUDY (Ferland et al. 2013, 2017) to compute the [C II] luminosity for a large number of galaxies at  $z \geq 4$ , Lagache et al. (2018, hereafter L18) reproduced the  $L_{\text{CII,SFR}} - \text{SFR}$  relation observed in high- $z$  star-forming galaxies. They found a mild evolution of the  $L_{\text{CII,SFR}} - \text{SFR}$  relation with redshift from  $z = 4$  to  $z = 7.6$ ,

$$\log L_{\text{CII,SFR}} = (7.1 - 0.07z) + (1.4 - 0.07z) \log(\text{SFR}), \quad (20)$$

with a scatter of about 0.5 dex.

De Looze et al. (2014) analysed the  $L_{\text{CII,SFR}} - \text{SFR}$  relation for low-metallicity dwarf galaxies based on Herschel observations (Madden et al. 2013) and found a local relation with  $\log A = 7.16$ ,  $\gamma = 1.25$  and 0.5 dex scatter (hereafter deL14d), i.e.

$$\log L_{\text{CII,SFR}} = 7.16 + 1.25 \log \text{SFR}, \quad (21)$$

De Looze et al. (2014) also obtained  $\log A = 7.22$ ,  $\gamma = 0.85$  and 0.3 dex scatter (hereafter deL14z) for high- $z$  samples with  $z = 0.59 - 6.60$ .

$$\log L_{\text{CII,SFR}} = 7.22 + 0.85 \log \text{SFR} \quad (22)$$

Olsen et al. (2017) obtained  $\log A = 6.69$  and  $\gamma = 0.58$ , with a scatter of  $\sim 0.15$  dex (here after O17) by combining cosmological zoom simulations of galaxies with SÍGAME (Olsen et al. 2015) to model [C II] emissions from 30 main-sequence galaxies at  $z \sim 6$ ,

$$\log L_{\text{CII,SFR}} = (6.69 \pm 0.10) + (0.58 \pm 0.11) \log \text{SFR}. \quad (23)$$

This is consistent with Leung et al. (2020) who predict  $\log A = 6.82$  and  $\gamma = 0.66$ , based on cosmological hydrodynamics simulations using the SIMBA suite plus radiative transfer calculations via an updated version of SÍGAME.

Vallini et al. (2015) combined high-resolution, radiative transfer cosmological simulations with a subgrid multiphase model of the ISM to model the [C II] emissions from diffuse neutral gas and

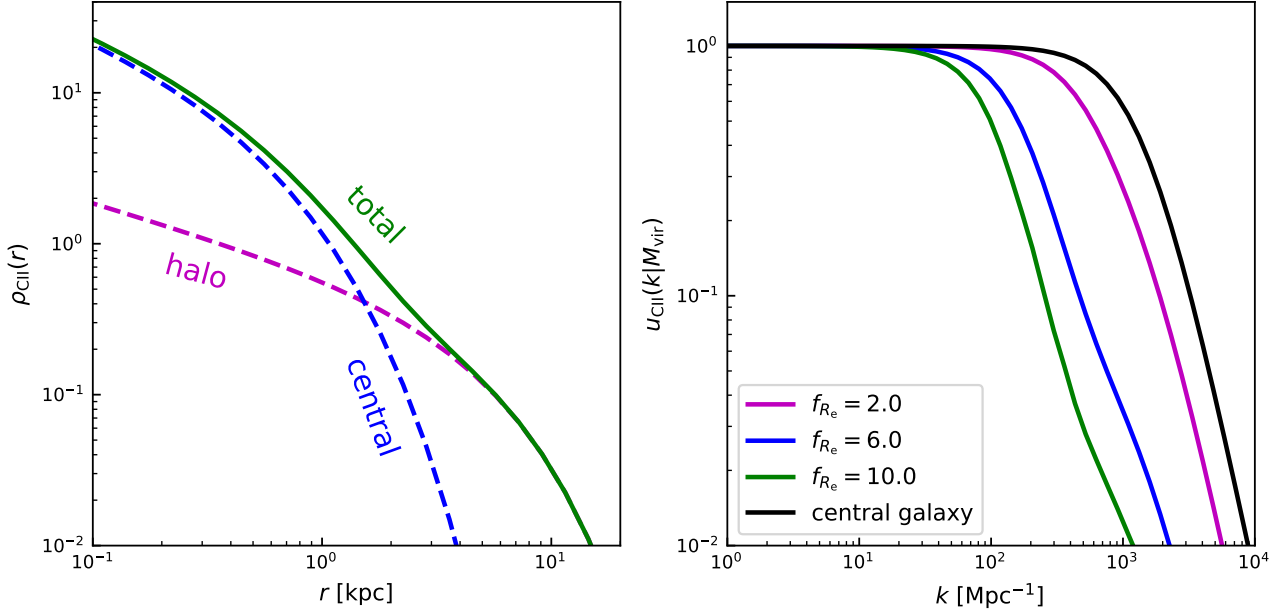


**Figure 1.** *Left:* The radial profile of a [C II] halo for dark matter halo mass  $M_{\text{vir}} = 10^{12} M_{\odot}$ ,  $f_{\Sigma} = 0.4$ ,  $f_{R_e} = 6.0$ . The blue and magenta dashed line is the profile for the central galaxy and halo part respectively, while the green solid line is the sum of these two components. *Right:* The corresponding normalized Fourier transform of the [C II] halo profile with different effective radius ratios  $f_{R_e}$ .

**Table 1.** Summary of  $L_{\text{CII,SFR}} - \text{SFR}$  relation parameters adopted in our model.

model	log A	$\gamma$	$\sigma_L$	Redshift	References
L18	6.68	0.98	0.60	6	Lagache et al. (2018)
deL14d	7.16	1.25	0.5	Local	De Looze et al. (2014)
deL14z	7.22	0.85	0.3	6.6	De Looze et al. (2014)
O17	6.69	0.58	0.15	6	Olsen et al. (2017)
V15	6.62	1.19	0.4	6.6	Vallini et al. (2015)
S20	6.61	1.17	0.28	4.4-5.9	Schaerer et al. (2020)

PDRs. By considering a physically-motivated metallicity, they found  $L_{\text{CII,SFR}} - \text{SFR}$  relation both depends on the SFR and metallicity and can be fitted by

$$\log L_{\text{CII,SFR}} = 7.0 + 1.2 \log(\text{SFR}) + 0.021 \log(Z) + 0.012 \log(\text{SFR}) \log(Z) - 0.74 \log^2(Z). \quad (24)$$

For  $Z = 0.2 Z_{\odot}$ , we obtain  $\log A = 6.62$  and  $\gamma = 1.19$  (here after V15).

Schaerer et al. (2020), using 118 galaxies at  $4.4 < z < 5.9$  from the ALMA ALPINE Large Program (Le Fèvre et al. 2020), obtain

$$\log L_{\text{CII,SFR}} = (6.61 \pm 0.2) + (1.17 \pm 0.12) \log \text{SFR}, \quad (25)$$

with a scatter of  $\sim 0.28$  dex (here after S20).

The parameters of the six  $L_{\text{CII,SFR}} - \text{SFR}$  relations adopted are summarized in Tab. 1. Since the observed  $\sigma_L$  involves both the observational uncertainties and the intrinsic scatters, and the simulated  $\sigma_L$  might be limited by the method of modeling the input physical properties scattering, for simplicity in this work we ignore the  $\sigma_L$ , and simply use  $\log L_{\text{CII,SFR}} = \log A + \gamma \log \text{SFR}$  in the following. We plot the corresponding  $L_{\text{CII,SFR}} - M_{\text{vir}}$  relations in Fig. 2.

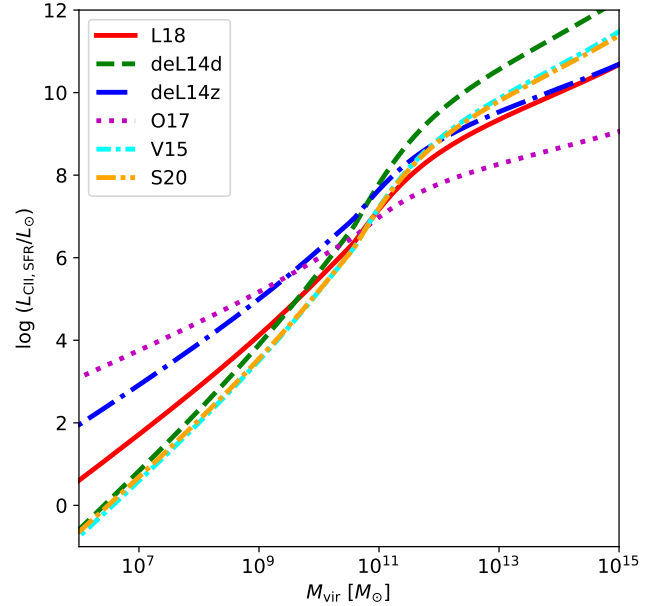


**Figure 2.** The  $L_{\text{CII,SFR}} - M_{\text{vir}}$  relation obtained from Abundance Matching method for six  $L_{\text{CII,SFR}} - \text{SFR}$  relations.

### 2.3 Modeling the power spectrum

The [C II] intensity mapping power spectrum comprises clustering and shot noise components. In the halo model framework, the clustering term can be split into one-halo and two-halo terms, which arise from the correlation within halos and the correlation between halos,

respectively:

$$P_{\text{CII}}(k, z) = P_{\text{CII}}^{\text{CL}}(k, z) + P_{\text{CII}}^{\text{SN}}(z) \\ = P_{\text{CII}}^{\text{1h}}(k, z) + P_{\text{CII}}^{\text{2h}}(k, z) + P_{\text{CII}}^{\text{SN}}(z), \quad (26)$$

where the shot noise  $P_{\text{CII}}^{\text{SN}}$  is generally independent of  $k$ . The one-halo term  $P_{\text{CII}}^{\text{1h}}(k, z)$  and the two-halo term  $P_{\text{CII}}^{\text{2h}}(k, z)$  depend on the large-scale structure, the normalized Fourier transform of the [C II] halo profile and the  $L_{\text{CII}, \text{SFR}} - M_{\text{vir}}$  relation.

The one-halo term<sup>3</sup>

$$P_{\text{CII}}^{\text{1h}}(k, z) = \int dM_{\text{vir}} \frac{dn}{dM_{\text{vir}}} u_{\text{CII}}(k|M_{\text{vir}})^2 \left[ \frac{L_{\text{CII}}(M_{\text{vir}}, z)}{4\pi D_L^2} y(z) D_c^2 \right]^2 \\ = \left( \frac{c}{4\pi \nu_{\text{CII}} H(z)} \right)^2 \int dM_{\text{vir}} \frac{dn}{dM_{\text{vir}}} [L_{\text{CII}}(M_{\text{vir}}, z) u_{\text{CII}}(k|M_{\text{vir}})]^2, \quad (27)$$

and two-halo term

$$P_{\text{CII}}^{\text{2h}}(k, z) = \left( \int dM_{\text{vir}} \frac{dn}{dM_{\text{vir}}} u_{\text{CII}}(k|M_{\text{vir}}) \right)^2 \left[ \frac{L_{\text{CII}}(M_{\text{vir}}, z)}{4\pi D_L^2} y(z) D_c^2 \right]^2 \\ = \left( \int dM_{\text{vir}} \frac{dn}{dM_{\text{vir}}} L_{\text{CII}}(M_{\text{vir}}, z) u_{\text{CII}}(k|M_{\text{vir}}) b_{\text{SMT}}(M_{\text{vir}}, z) \right)^2 \text{ along the line of sight, where } \delta \nu_0 \text{ is the frequency resolution; and between} \\ \times \left( \frac{c}{4\pi \nu_{\text{CII}} H(z)} \right)^2 P(k, z). \quad (28)$$

$D_L$  is the luminosity distance and  $D_c$  is the comoving distance to redshift  $z$ .  $y(z) = c(1+z)/[\nu_0 H(z)]$  is the derivative of the comoving radial distance with respect to the observed frequency  $\nu_0$ , which is related to the rest-frame frequency of [C II] line as  $\nu_0 = \nu_{\text{CII}}/(1+z)$ ;  $c$  is the light speed and  $H(z)$  is the Hubble parameter. We adopt the Sheth-Tormen form (Sheth & Tormen 1999) of the halo mass function  $dn/dM_{\text{vir}}$ , the Eisenstein & Hu (1999) form of the linear matter power spectrum  $P(k, z)$ , and the Sheth et al. (2001) form of dark matter halo bias  $b_{\text{SMT}}(M_{\text{vir}}, z)$ .  $L_{\text{CII}}(M_{\text{vir}}, z) = L_{\text{CII}, \text{g}} + L_{\text{CII}, \text{h}}$  is the [C II] luminosity of the dark matter halo with mass  $M_{\text{vir}}$ , including the central galaxy and the extended [C II] halo.

Finally, the Poissonian shot noise, arising from the discrete nature of dark matter halos, can be computed as

$$P_{\text{CII}}^{\text{SN}}(z) = \left( \frac{c}{4\pi \nu_{\text{CII}} H(z)} \right)^2 \int dM_{\text{vir}} \frac{dn}{dM_{\text{vir}}} L_{\text{CII}}^2(M_{\text{vir}}, z) \quad (29)$$

The integration of Eqs. (27, 28 & 29) is performed between  $M_{\text{min}}$  and  $M_{\text{max}}$ . We set  $M_{\text{min}} = 10^8 M_{\odot}$ , which is roughly the atomic cooling threshold (the virial mass corresponding to virial temperature  $10^4$  K) at redshift 6. This is the minimum mass that can sustain persistent star formation activity. Suppose the survey volume is  $V_{\text{survey}}$ , then in such volume the mean number of dark matter halos with mass  $M_{\text{vir}}$  is

$$\bar{n} V_{\text{survey}} \sim M_{\text{vir}} \frac{dn}{dM_{\text{vir}}} V_{\text{survey}}. \quad (30)$$

In  $V_{\text{survey}}$ , the probability to find at least one dark matter halo with mass  $\sim M_{\text{vir}}$  is  $G(\geq 1|\bar{n} V_{\text{survey}})$ , where  $G$  is the cumulative Poisson

<sup>3</sup> The one halo term formula of Eq. (27) tends to be a constant at large scale (low- $k$ ), this is an unphysical behavior (Schaan & White 2021). Some attempts have been proposed to solve the problem (Cooray & Sheth 2002; Baldauf et al. 2013), but it is still an open issue.

probability with mean value  $\bar{n} V_{\text{survey}}$ . We obtain  $M_{\text{max}}$  by solving the equation  $G(\geq 1|\bar{n} V_{\text{survey}}) = 0.5$ , which means in the volume  $V_{\text{survey}}$  the contribution from dark matter halos whose existence probability smaller than 50% is excluded. This is to avoid such bright and rare objects biasing our results. When  $V_{\text{survey}} = 10^6 \text{ Mpc}^3$ ,  $M_{\text{max}} \sim 5.5 \times 10^{12} M_{\odot}$  at redshift 6.

## 2.4 The signal-to-noise ratio estimation

If a survey has an angular area  $\Omega_{\text{survey}}$  and a frequency range  $[\nu_0 - \Delta \nu_0, \nu_0]$  then it can detect the Fourier modes between

$$k_{\parallel, \text{min}} = \frac{2\pi}{\Delta r_{\parallel, \text{max}}} \\ \approx \frac{2\pi}{\frac{c(1+z)}{H(z)} \frac{\Delta \nu_0}{\nu_0}}, \quad (31)$$

and

$$k_{\parallel, \text{max}} = \frac{\pi}{\Delta r_{\parallel, \text{min}}} \\ \approx \frac{\pi}{\frac{c(1+z)}{H(z)} \frac{\delta \nu_0}{\nu_0}} \quad (32)$$

between

$$k_{\perp, \text{min}} = \frac{2\pi}{\Delta r_{\perp, \text{max}}} \\ \approx \frac{2\pi}{D_c(z) \sqrt{\Omega_{\text{survey}}}} \quad (33)$$

and

$$k_{\perp, \text{max}} = \frac{\pi}{\Delta r_{\perp, \text{min}}} \\ \approx \frac{\pi}{D_c(z) \sqrt{\Omega_{\text{beam}}}} \quad (34)$$

transverse to the line of sight. Here  $z = \nu_{\text{CII}}/\nu_0 - 1$ ,  $\Omega_{\text{beam}}$  is the angular area of the beam. The survey detects the isotropic power spectrum in the range  $k_{\text{min}} < k < k_{\text{max}}$ , for which  $k_{\text{min}} \approx \sqrt{k_{\parallel, \text{min}}^2 + k_{\perp, \text{min}}^2}$  and  $k_{\text{max}} \approx \sqrt{k_{\parallel, \text{max}}^2 + k_{\perp, \text{max}}^2}$ .

The variance of the power spectrum measured in the above LIM survey is

$$\sigma_P^2(k) = \frac{1}{N_m(k)} [P_{\text{CII}}(k, z) W(k) + P_N]^2, \quad (35)$$

where the window function (Battye et al. 2013)

$$W(k) = \exp \left[ -\frac{1}{2} k^2 D_c^2(z) \frac{\Omega_{\text{beam}}}{4} \right] \quad (36)$$

denotes the rapid decline of the measured power spectrum below the resolution.  $P_N$  is the instrumental noise power spectrum.  $N_m(k)$  is the number of  $k$  modes sampled by a survey in the  $k$ -bin, which is given by

$$N_m(k) \approx 2\pi k^3 d \ln k \frac{V_{\text{survey}}}{(2\pi)^3}, \quad (37)$$

where  $d \ln k$  is the relative width of the selected  $k$ -bin<sup>4</sup>, and  $V_{\text{survey}}$  is the survey volume,

$$V_{\text{survey}} \approx D_c^2(z) \Omega_{\text{survey}} \left[ \frac{c(1+z)}{H(z)} \frac{\Delta \nu_0}{\nu_0} \right]. \quad (38)$$

<sup>4</sup> Throughout this paper, we adopt bin width  $d \ln k = 0.2$ .



Then the signal-to-noise ratio (S/N) of each  $k$ -bin

$$\begin{aligned} S/N &= \frac{P_{\text{CII}}(k, z)W^2(k)}{\sigma_P(k)} \\ &= \sqrt{N_m(k)} \frac{P_{\text{CII}}(k, z)W^2(k)}{P_{\text{CII}}(k, z)W^2(k) + P_N}, \end{aligned} \quad (39)$$

and the total signal-to-noise is

$$(S/N)_{\text{tot}} = \left( \sum_i \frac{P_{\text{CII}}^2(k_i)W^2(k_i)}{\sigma_P^2(k_i)} \right)^{1/2}, \quad (40)$$

where the sum is performed for all  $k$ -bins.

If the instrumental noise flux is  $\sigma_N$ , the instrumental noise power spectrum is

$$P_N = \left( \frac{\sigma_N}{\Omega_{\text{beam}}} \right)^2 V_{\text{vox}}, \quad (41)$$

where

$$V_{\text{vox}} \approx D_c^2(z) \Omega_{\text{beam}} \left[ \frac{c(1+z)}{H(z)} \frac{\delta\nu_0}{\nu_0} \right], \quad (42)$$

is the comoving volume of the real space voxel.

Suppose the survey is carried out by an interferometer array with  $N_{\text{an}}$  antennas, each antenna has diameter  $d$  and system temperature  $T_{\text{sys}}$ , then the instrumental noise flux

$$\sigma_N = \frac{2k_B T_{\text{sys}}}{d^2 \sqrt{N_{\text{an}}(N_{\text{an}} - 1)/2\delta\nu_0 t_{\text{int}}}}, \quad (43)$$

where  $t_{\text{int}}$  is the integration time on source. If the total observation time is  $t_{\text{obs}}$ , and there are  $N_{\text{chn}}$  frequency channels, then

$$t_{\text{int}} = \frac{t_{\text{obs}}}{V_{\text{survey}}/V_{\text{vox}}/N_{\text{an}}/N_{\text{chn}}}. \quad (44)$$

If the interferometer has maximum baseline length  $b_{\text{max}}$ , then the Full Width at Half Maximum (FWHM) of the beam is  $\theta_{\text{FWHM}} = 1.2\lambda_{\text{obs}}/b_{\text{max}}$ , for Gaussian profile  $\theta_{\text{beam}} = \theta_{\text{FWHM}}/\sqrt{2\ln 2}$ , hence  $\Omega_{\text{beam}} = (\theta_{\text{beam}})^2 = (\theta_{\text{FWHM}}/\sqrt{2\ln 2})^2$ .

### 3 RESULTS

#### 3.1 [C II] power spectrum

In Fig. 3, we plot the intensity mapping power spectrum at  $z \sim 6$  for the six  $L_{\text{SFR,CII}} - \text{SFR}$  relations with effective radius ratio values  $f_{R_e} = [2.0, 6.0, 10.0]$ , representing conservative, moderate, and extreme cases, respectively. We fix  $f_{\Sigma} = 0.4$ , i.e. the central surface brightness of the halo represents  $\sim 30\%$  of the total, which is a reasonable guess from the fitting results of the observational data (Akens et al. 2022). It clearly shows that [C II] halos largely boost the intensity of the power spectrum. Compared with the power spectrum of central galaxies, the signal is boosted by  $\sim 20, 10^3, 10^4$  times when  $f_{R_e} = 2.0, 6.0, 10.0$  independently on the specific form of  $L_{\text{CII,SFR}} - \text{SFR}$  relations. Moreover, [C II] halos imprint a specific signature in the one-halo term at small scales. Since the central galaxy is more compact, the typical turnover scale of the one-halo term is  $\sim 10^3 \text{ Mpc}^{-1}$ . However, the [C II] halo is more extended and the typical turnover scale is shifted to  $\sim 100 \text{ Mpc}^{-1}$ . However, this feature is generally buried in the shot noise, which is the generally dominant component at the smallest scales. Fig. 4 illustrates instead the power spectrum dependence on  $f_{\Sigma}$  at a fixed value of  $f_{R_e} = 6.0$ . We show the results for  $f_{\Sigma} = 0.1, 0.4$ , where the signal is strengthened by  $\sim 10^2, 10^3$  times, respectively.

We also explore the results in the  $f_{R_e} - f_{\Sigma}$  parameter space, as shown in Fig. 5. We plot the values of the total power spectrum,  $P_{\text{CII}}$ , at  $k = 0.3 \text{ Mpc}^{-1}$  by varying  $f_{\Sigma}$  and  $f_{R_e}$  simultaneously. To avoid repetition, we only show the result for the L18 relation. As we can see,  $P_{\text{CII}}$  is sensitive to both changes in  $f_{R_e}$  and in  $f_{\Sigma}$ .

#### 3.2 Detectability of the [C II] halo signal

We now turn the discussion to the detectability of the predicted [C II] power spectrum signal in a LIM survey.

##### 3.2.1 Detectability in ALMA ASPECS Survey

The ALMA Large Program ASPECS (Aravena et al. 2020) surveying the Hubble Ultra Deep Field (HUDF) provides the first full frequency scan in Band 6, corresponding to the frequency window for [C II] emission from  $6 < z < 8$  galaxies, we first consider the detectability of [C II] power spectrum signal by such an experiment.

The ASPECS Band 6 data covers a total area of  $4.2 \text{ arcmin}^2$  in the HUDF, with  $2.9 \text{ arcmin}^2$  area within the 50% primary beam response (Decarli et al. 2020). The observed frequency range is  $212 - 272 \text{ GHz}$ , corresponding to the redshift range  $z = 5.99 - 7.97$  for the [C II] line. If we rebin the frequency channels by a factor of 8, as suggested by Uzgil et al. (2021), the spectral resolution is  $\delta\nu_0 = 62.5 \text{ MHz}$ . The synthesized beam size (the FWHMs of the pixel ellipse along its major and minor axes, see Uzgil et al. 2019) in the image cube is  $\Delta\theta_{b,\text{maj}} \times \Delta\theta_{b,\text{min}} = 1.6'' \times 1.1''$  (Uzgil et al. 2021). Then

$$\Omega_{\text{beam}} = \frac{\theta_{b,\text{maj}} \times \theta_{b,\text{min}}}{2 \ln 2}. \quad (45)$$

From these survey parameters, we derive  $k_{\parallel,\text{min}} = 0.009 \text{ Mpc}^{-1}$ ,  $k_{\parallel,\text{max}} = 4.551 \text{ Mpc}^{-1}$ ,  $k_{\perp,\text{min}} = 1.503 \text{ Mpc}^{-1}$ , and  $k_{\perp,\text{max}} = 68.147 \text{ Mpc}^{-1}$ , and we finally have  $k_{\text{min}} = 1.503 \text{ Mpc}^{-1}$ ,  $k_{\text{max}} = 68.299 \text{ Mpc}^{-1}$ . We summarize the ASPECS survey parameters derived for the [C II] power spectrum analysis in Tab. 2.

Next, we compute the S/N of the [C II] power spectrum for an ASPECS-like survey. The survey has noise flux  $\sigma_N = 0.30 \text{ mJy beam}^{-1}$  (Uzgil et al. 2021), which yields a surface brightness intensity sensitivity  $\sigma_N/\Omega_{\text{beam}} = 1.01 \times 10^7 \text{ Jy sr}^{-1}$ , and a noise power spectrum  $P_N = 1.48 \times 10^{11} (\text{Jr/sr})^2 \text{ Mpc}^3$  using Eq. (41).

We show the results of S/N for various  $L_{\text{CII,SFR}} - \text{SFR}$  relations with  $f_{\Sigma} = 0.4$ ,  $f_{R_e} = 2.0$  (left panel, represents a relatively compact [C II] halo) and  $f_{\Sigma} = 0.1$ ,  $f_{R_e} = 6.0$  (right panel, represents a relatively diffuse [C II] halo) respectively in Fig. 6. In the left panel, only the signal of the deL14d [C II] - SFR model is detectable (with  $S/N \gtrsim 3$ ) in the range  $4 \text{ Mpc}^{-1} \lesssim k \lesssim 70 \text{ Mpc}^{-1}$ . In the right panel, the model deL14d is detectable in  $1 \text{ Mpc}^{-1} \lesssim k \lesssim 70 \text{ Mpc}^{-1}$ , while the models deL14z, V15, and S20 are detectable in  $10 \text{ Mpc}^{-1} \lesssim k \lesssim 70 \text{ Mpc}^{-1}$ . This is because although the surface brightness of the [C II] halo is lower in the right panel, the total luminosity is larger as it scales with  $f_{R_e}^2$ .

##### 3.2.2 Optimal survey strategy

To optimally probe the extended [C II] halo signal, an ideal survey should be able to detect the signal with a resolution up to scale comparable to the extended [C II] halo size. On the other hand, to enhance the statistical significance of the signal, the survey should cover a sky area much larger than the ASPECS. Here we propose, by using ALMA 12-m antennas in an extended configuration with  $\sim 1000 \text{ m}$  baseline,  $N_{\text{an}} = 500$ , and  $N_{\text{chn}} = 1000$ , to survey a

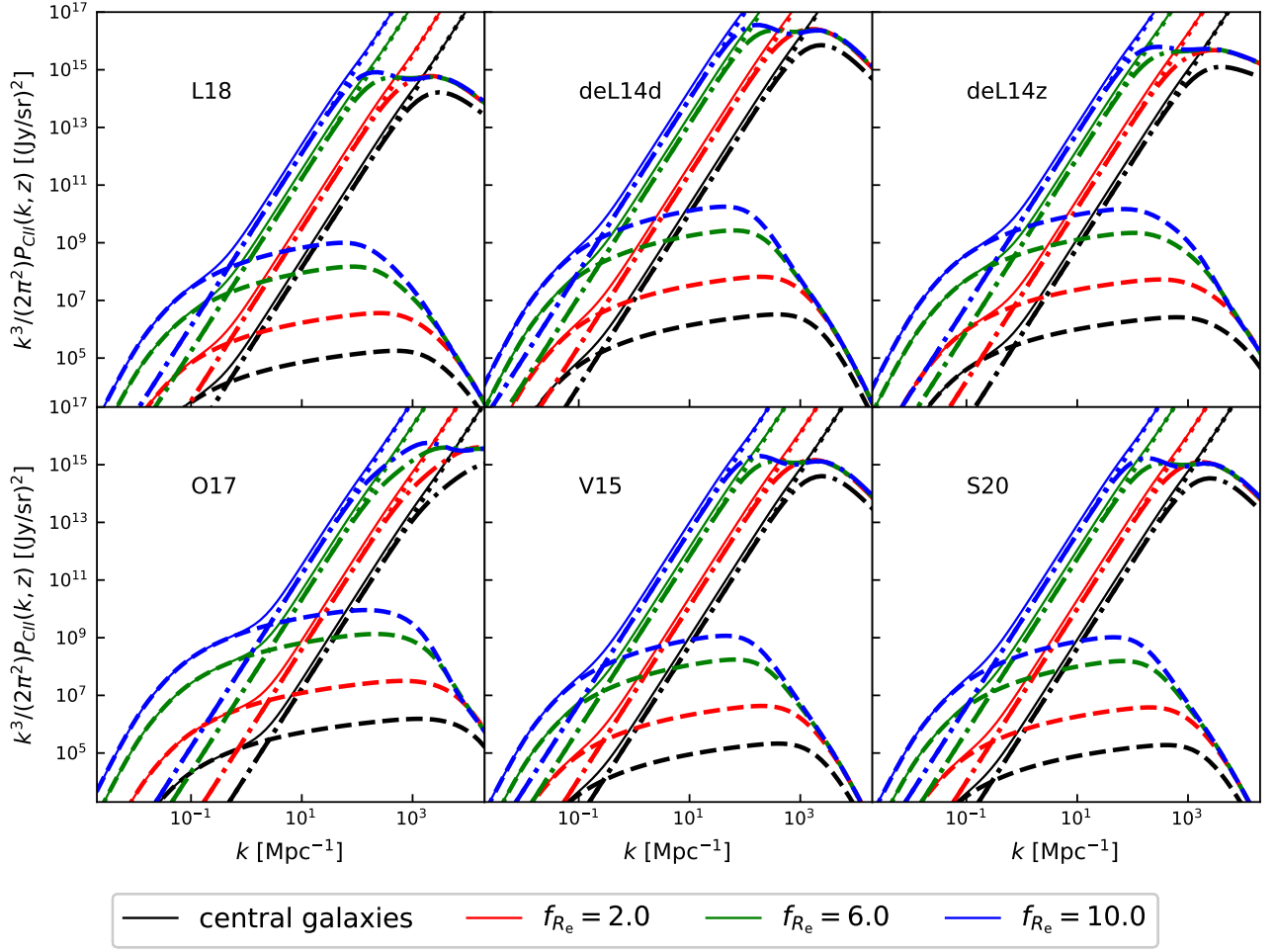


**Figure 3.** Predicted [C II] power spectrum for six [C II]-SFR relations. The dash-dotted line, dashed line, dotted line, and thin solid line denote the one-halo, two-halo, shot noise terms, and sum of them respectively, in both panels. The dotted line (shot noise) overlaps with the dash-dotted line (one-halo term) at a large scale. The black line represents the [C II] power spectrum for the central galaxy, i.e. without [C II] halo considered. Red, green, and blue lines corresponding to  $f_{R_e} = [2.0, 6.0, 10.0]$ , with fixed  $f_{\Sigma} \sim 0.4$ .

**Table 2.** The ASPECS survey parameters for S/N analysis.

$[\nu_0 - \Delta\nu_0, \nu_0]$	[212–272] GHz
$z$	[5.99, 7.97]
$\delta\nu_0$	62.5 MHz
$\Omega_{\text{survey}}$	2.9 arcmin <sup>2</sup>
$\Omega_{\text{beam}}$	1.6'' × 1.1''
$\sigma_N$	0.30 mJy beam <sup>-1</sup>
$V_{\text{survey}}$	13260 Mpc <sup>3</sup>
$\Delta r_{\parallel, \text{min}}$	0.690 Mpc
$\Delta r_{\parallel, \text{max}}$	662.701 Mpc
$\Delta r_{\perp, \text{min}}$	0.046 Mpc
$\Delta r_{\perp, \text{max}}$	4.180 Mpc
$k_{\parallel, \text{min}}$	0.009 Mpc <sup>-1</sup>
$k_{\parallel, \text{max}}$	4.551 Mpc <sup>-1</sup>
$k_{\perp, \text{min}}$	1.503 Mpc <sup>-1</sup>
$k_{\perp, \text{max}}$	68.299 Mpc <sup>-1</sup>
$k_{\text{min}}$	1.503 Mpc <sup>-1</sup>
$k_{\text{max}}$	68.299 Mpc <sup>-1</sup>
$P_N$	$1.48 \times 10^{11}$ (Jy/sr) <sup>2</sup> Mpc <sup>3</sup>

total area of  $\Omega_{\text{survey}} \sim 2 \text{ deg}^2$  in frequency band [212–272] GHz with total observing time  $t_{\text{obs}} \sim 1000 \text{ hr}$ . The frequency resolution  $\delta\nu_0 = \Delta\nu_0/N_{\text{chn}} = 60 \text{ MHz}$ .

The system temperature<sup>5</sup> of ALMA at observing frequency  $\nu_0 = 272 \text{ GHz}$  is  $T_{\text{sys}} \sim 115 \text{ K}$ . Following the procedures in Section 2.4, we calculate the S/N and show them in Fig. 7. A summary of the parameters for this designed survey is given in Tab. 3.

For this optimized survey, when  $f_{\Sigma} = 0.4$  and  $f_{R_e} = 2.0$  (see the left panel of Fig. 7), the [C II] power spectra of the four  $L_{\text{CII, SFR}} - \text{SFR}$  relations deL14d, deL14z, V15 and S20 models are all detectable with total signal-to-noise ratio  $\geq 10$ , while the L18 relation is just marginally detectable, and the O17 relation is not detectable. For the more extended [C II] halo model with  $f_{\Sigma} = 0.1$  and  $f_{R_e} = 6.0$  (see the right panel of Fig. 7), the power spectra are detectable with total signal-to-noise ratio  $\geq 10$  for all the five  $L_{\text{CII, SFR}} - \text{SFR}$  relations, except for O17 whose S/N is just  $\sim 3$ .

<sup>5</sup>  $T_{\text{sys}}$  comes from the [ALMA Sensitivity Calculator \(ASC\)](#) by setting the observing frequency  $\nu_0 = 272 \text{ GHz}$  and bandwidth  $\Delta\nu_0 = 60 \text{ GHz}$ .

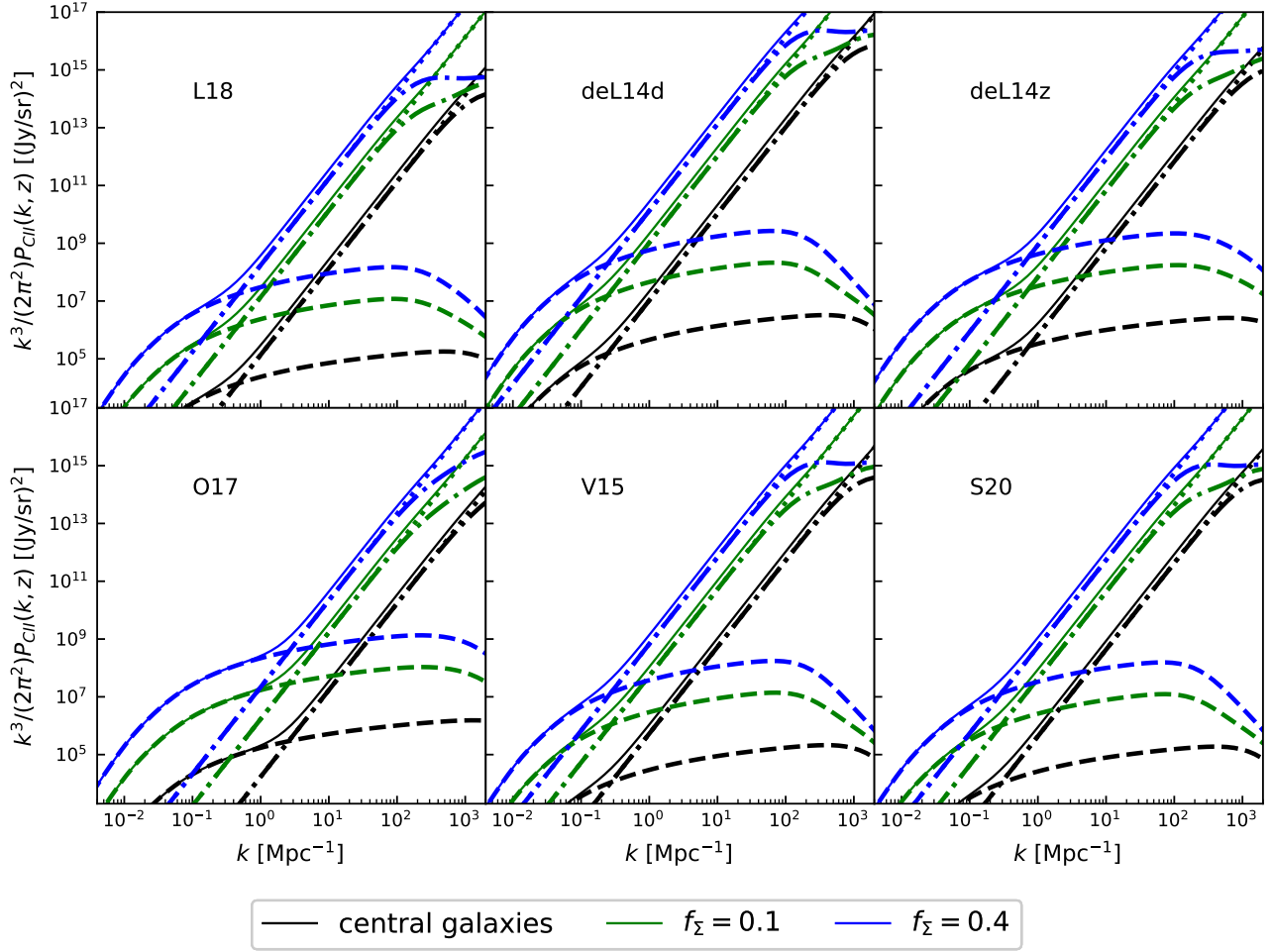


**Figure 4.** As in Fig. 3 for different values of  $f_z$  and for the six different [C II] -SFR relations considered (see Tab. 1); we fix  $f_{R_e} = 6.0$  here.

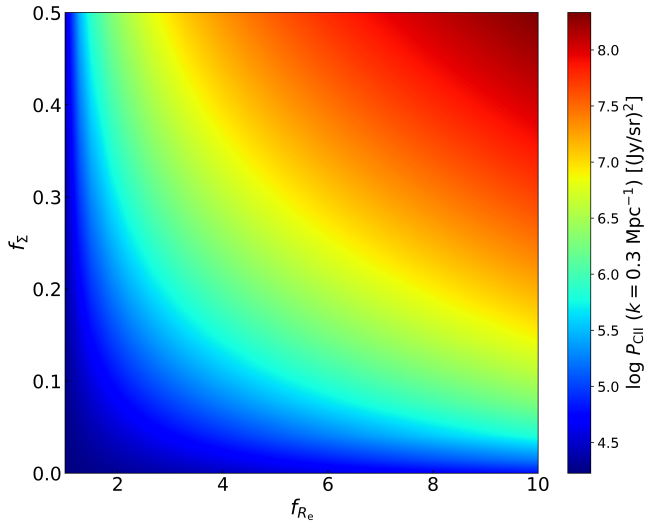


**Figure 5.** The total [C II] halo power spectrum at  $k = 0.3 \text{ Mpc}^{-1}$  as a function of  $f_z$  and  $f_{R_e}$ , to avoid repetition we only show the result for L18 [C II] -SFR relation.

**Table 3.** Parameters of a designed optimal survey

$d$	12 m
$T_{\text{sys}}$	115 K
$N_{\text{an}}$	500
$N_{\text{chn}}$	1000
$b_{\text{max}}$	1000 m
$\theta_{\text{beam}}$	0.232''
$[\nu_0 - \Delta\nu_0, \nu_0]$	[212, 272] GHz
Redshift range	[6.0-8.0]
$\delta\nu_0$	60 MHz
$t_{\text{obs}}$	1000 hr
$\Omega_{\text{survey}}$	2 deg <sup>2</sup>
$V_{\text{survey}}$	$2.88 \times 10^7 \text{ Mpc}^3$
$V_{\text{vox}}$	$5.96 \times 10^{-5} \text{ Mpc}^3$
$P_N$	$6.52 \times 10^{12} (\text{Jy sr}^{-1})^2 \text{ Mpc}^3$
$k_{\text{min}}$	0.032 $\text{Mpc}^{-1}$
$k_{\text{max}}$	331.43 $\text{Mpc}^{-1}$

### 3.2.3 Constraining the [C II] halo parameters

We have shown that when the contribution from extended [C II] halos is considered, the [C II] power spectrum is boosted. However, this is mainly because the total [C II] luminosity of the system (central



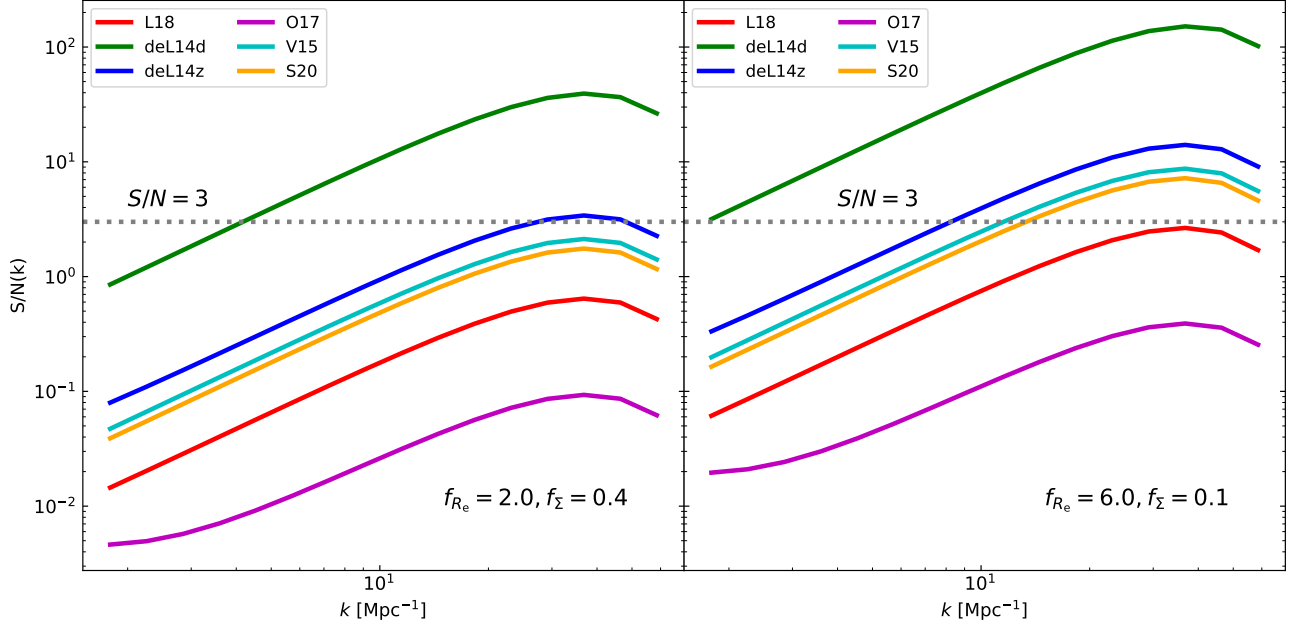


**Figure 6.** Signal-to-noise ratio for six different  $L_{\text{CII,SFR}} - \text{SFR}$  relations for the ALMA ASPECS Survey. *Left panel:* case with  $f_{R_e} = 2.0$ ,  $f_{\Sigma} = 0.4$ . *Right panel:* same for  $f_{R_e} = 6.0$ ,  $f_{\Sigma} = 0.1$ .

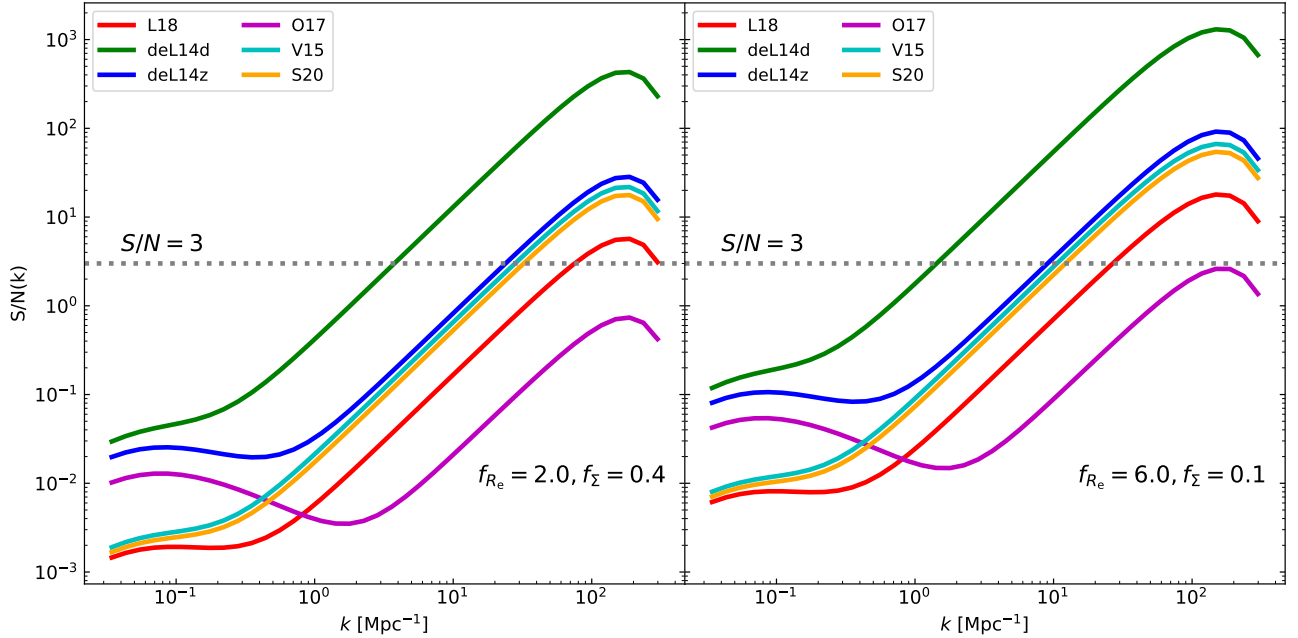


**Figure 7.** As in Fig. 6 but for the optimal survey strategy by using ALMA. With 1000 m baseline, the largest  $k$  mode can be probed is  $k_{\text{max}} = 331.43 \text{ Mpc}^{-1}$ . Except for O17 relation, the signal for the other five  $L_{\text{CII,SFR}} - \text{SFR}$  relations can be detected by this configuration when  $f_{\Sigma} = 0.4$  and  $f_{R_e} = 2.0$ .

galaxy + [C II] halo) is larger. So there is a degeneracy between the [C II] halo contribution and the [C II] - SFR relation. [C II] halos also change the shape of the [C II] power spectrum (one-halo term) at scales comparable to their size. However, the scales are so small, generally, the shot noise is much larger than the one-halo term. Here we investigate whether our designed optimal survey is able to put some conclusive constraints on the [C II] halo properties.

In Fig. 8 we show the forecast on the constraints of [C II] halo parameters for our designed optimal survey. This is obtained by

minimizing

$$\chi^2(\theta) = \sum_{i=1}^{N_{\text{bin}}} \frac{\left[ P_{\text{CII}}(k_i, \theta) W^2(k_i) - P_{\text{CII}}^{\text{obs}}(k_i) W^2(k_i) \right]^2}{\sigma_P^2(k_i)} \quad (46)$$

using the MCMC procedure (Goodman & Weare 2010), where  $\theta = \{\log A, \gamma, f_{\Sigma}, f_{R_e}\}$  represents the  $L_{\text{CII,SFR}} - \text{SFR}$  relation and extended [C II] halo parameters;  $N_{\text{bin}}$  is the number of  $k$  bins between  $k_{\text{min}}$  and  $k_{\text{max}}$ , with width  $d \ln k = 0.2$ ;  $P_{\text{CII}}^{\text{obs}}$  is the mock

observed power spectrum generated by adopting  $\log A = 6.5$ ,  $\gamma = 1.2$ ,  $f_{\Sigma} = 0.1$  and  $f_{R_e} = 6.0$ . The mock uncertainty of the observed power spectrum is given by Eq. (35). When performing the MCMC procedure, we set flat priors  $\log A \in [5.0, 9.0]$ ,  $\gamma \in [0.1, 2.0]$ ,  $f_{\Sigma} \in [0.0, 0.5]$ ,  $f_{R_e} \in [1.0, 10.0]$ . The marginalized parameters for [C II] halo are:  $f_{\Sigma} = 0.24^{+0.17}_{-0.14}$ ,  $f_{R_e} = 6.08^{+1.56}_{-1.24}$ . Indeed, it is feasible to distinguish the extended [C II] halo contribution to the power spectrum in this designed optimal survey. However, we also check that the ASPECS survey is still hard to give conclusive constraints, because of the smaller S/N and lower resolution.

#### 4 CONCLUSIONS

In this paper, we predicted the foreground- and contamination-cleaned [C II] power spectrum signal at  $z \approx 6$ , when both central galaxies and extended [C II] halos are considered, and investigate the detectability of such signal using ALMA ASPECS survey and a designed optimized survey. We modeled the [C II] luminosity profiles of the central galaxy and extended [C II] halo by a Sérsic+exponential profile, and derive the [C II] - dark matter halo mass relation by matching the dark matter halo mass function with dust-corrected UV luminosity function of high-redshift galaxies. The main results are:

- The extended [C II] halos around high redshift galaxies can significantly enhance the LIM signal compared with the signal produced by central galaxies alone, both in terms of the clustering signal and shot noise.
- Our [C II] halo model has two free parameters: the effective [C II] halo/galaxy radius ratio,  $f_{R_e}$ , and the central surface brightness ratio,  $f_{\Sigma}$ . The luminosity of extended [C II] halos is  $\sim 2.24 f_{\Sigma} f_{R_e}^2$  times the central galaxies. When the [C II] halo contribution is included, compared with the power spectrum from central galaxies only, the signal is boosted by a factor from  $\sim 20$  to  $\sim 10^3$  when  $f_{R_e}$  varies between 2.0 to 6.0, if  $f_{\Sigma} = 0.4$ . Given  $f_{R_e} = 6.0$ , the power spectrum is enhanced by  $\sim 100$  to  $\sim 10^3$  times when  $f_{\Sigma}$  changes from 0.1 to 0.4.
- For a LIM experiment configured as the ALMA ASPECS Large Program (with resolution  $\theta_{\text{beam}} = 1.13''$  and survey area  $\Omega_{\text{survey}} = 2.9 \text{ arcmin}^2$ ), the [C II] power spectrum signal is detectable ( $S/N \gtrsim 3$ ) for the deL14d  $L_{\text{CII,SFR}} - \text{SFR}$  relation with  $f_{\Sigma} = 0.4$  and  $f_{R_e} = 2.0$ , and for the deL14d, deL14z, V15 and S20 relations with  $f_{\Sigma} = 0.1$  and  $f_{R_e} = 6.0$ . So for a LIM experiment, the signal of more extended, low surface brightness [C II] halos is more easily detected.
- To optimally detect the signal, we proposed an optimized survey using more ALMA antennas and longer baselines. The survey has a higher resolution ( $\theta_{\text{beam}} \sim 0.232''$ ) and larger survey area ( $\Omega_{\text{survey}} \sim 2 \text{ deg}^2$ ). The resulting signal-to-noise ratio is large enough so that the signal from five out of six  $L_{\text{CII,SFR}} - \text{SFR}$  relations, except for the O17 relation, is detectable. We also predicted the confidence levels of the constraints on the  $L_{\text{CII,SFR}} - \text{SFR}$  relation and [C II] halo parameters by this optimized survey. These two halo parameters are degenerate, but we still expect to obtain meaningful constraints, with uncertainties of 60% (20%) on  $f_{\Sigma}$  ( $f_{R_e}$ ).

In this work we ignored the continuum foreground and intervening lines, assuming they could be perfectly removed and a clean [C II] signal is obtained. It is beyond the scope of this work to explore in detail foreground removal algorithms. A method for foreground and contamination subtraction has been discussed in Yue et al. (2015); Yue & Ferrara (2019).

Our predictions depend on the effective radius ratio, the central

surface brightness ratio, and the choice of the  $L_{\text{CII,SFR}} - \text{SFR}$  relation. Therefore, detection of the [C II] halo signal in the LIM power spectrum can be used to verify whether [C II] halos are ubiquitous in high-redshift galaxies, and provide information about [C II] halo size, and their possible relation with outflows carrying the emitting material out of the main galaxy body. Finally, it can be potentially used to constrain the  $L_{\text{CII,SFR}} - \text{SFR}$  relation at high- $z$  as the amplitude of the power spectrum is sensitive to such quantity.

#### ACKNOWLEDGEMENTS

MZ acknowledges the financial support from the China Scholarship Council (CSC, No.202104910322). AF acknowledges support from the ERC Advanced Grant INTERSTELLAR H2020/740120. Partial support from the Carl Friedrich von Siemens-Forschungspreis der Alexander von Humboldt-Stiftung Research Award is kindly acknowledged. BY acknowledges the support by the National SKA Program of China No. 2020SKA0110402. We gratefully acknowledge computational resources of the Center for High Performance Computing (CHPC) at SNS. We make use of Scipy (Virtanen et al. 2020), Numpy (Harris et al. 2020), Matplotlib (Hunter 2007), emcee (Foreman-Mackey et al. 2013), and corner (Foreman-Mackey 2016) package for Python to do the calculation and produce the plot.

#### DATA AVAILABILITY

The data produced in this study are available from the corresponding author upon reasonable request.

#### REFERENCES

- Akins H. B., et al., 2022, *ApJ*, **934**, 64  
 Aravena M., Carilli C., Decarli R., Walter F., ASPECS Collaboration 2020, *The Messenger*, **179**, 17  
 Baes M., Gentile G., 2011, *A&A*, **525**, A136  
 Bakx T. J. L. C., et al., 2020, *MNRAS*, **493**, 4294  
 Baldauf T., Seljak U., Smith R. E., Hamaus N., Desjacques V., 2013, *Phys. Rev. D*, **88**, 083507  
 Battye R. A., Browne I. W. A., Dickinson C., Heron G., Maffei B., Pourtsidou A., 2013, *MNRAS*, **434**, 1239  
 Binney J., Mamon G. A., 1982, *MNRAS*, **200**, 361  
 Binney J., Tremaine S., 1987, *Galactic dynamics*  
 Bouwens R. J., et al., 2015, *ApJ*, **803**, 34  
 Breyse P. C., Kovetz E. D., Kamionkowski M., 2014, *MNRAS*, **443**, 3506  
 Bruzual G., Charlot S., 2003, *MNRAS*, **344**, 1000  
 Capak P. L., et al., 2015, *Nature*, **522**, 455  
 Carniani S., et al., 2017, *A&A*, **605**, A42  
 Carniani S., et al., 2018, *MNRAS*, **478**, 1170  
 Castellano M., et al., 2016, *ApJ*, **818**, L3  
 Chabrier G., 2003, *PASP*, **115**, 763  
 Chang T.-C., Pen U.-L., Bandura K., Peterson J. B., 2010, arXiv e-prints, p. arXiv:1007.3709  
 Comaschi P., Ferrara A., 2016, *MNRAS*, **455**, 725  
 Cooray A., Sheth R., 2002, *Phys. Rep.*, **372**, 1  
 Dayal P., Ferrara A., 2018, *Phys. Rep.*, **780**, 1  
 De Looze I., et al., 2014, *A&A*, **568**, A62  
 Decarli R., et al., 2020, *ApJ*, **902**, 110  
 Eisenstein D. J., Hu W., 1999, *ApJ*, **511**, 5  
 Ferland G. J., et al., 2013, *Rev. Mex. Astron. Astrofis.*, **49**, 137  
 Ferland G. J., et al., 2017, *Rev. Mex. Astron. Astrofis.*, **53**, 385  
 Foreman-Mackey D., 2016, *The Journal of Open Source Software*, **1**, 24  
 Foreman-Mackey D., Hogg D. W., Lang D., Goodman J., 2013, *PASP*, **125**, 306

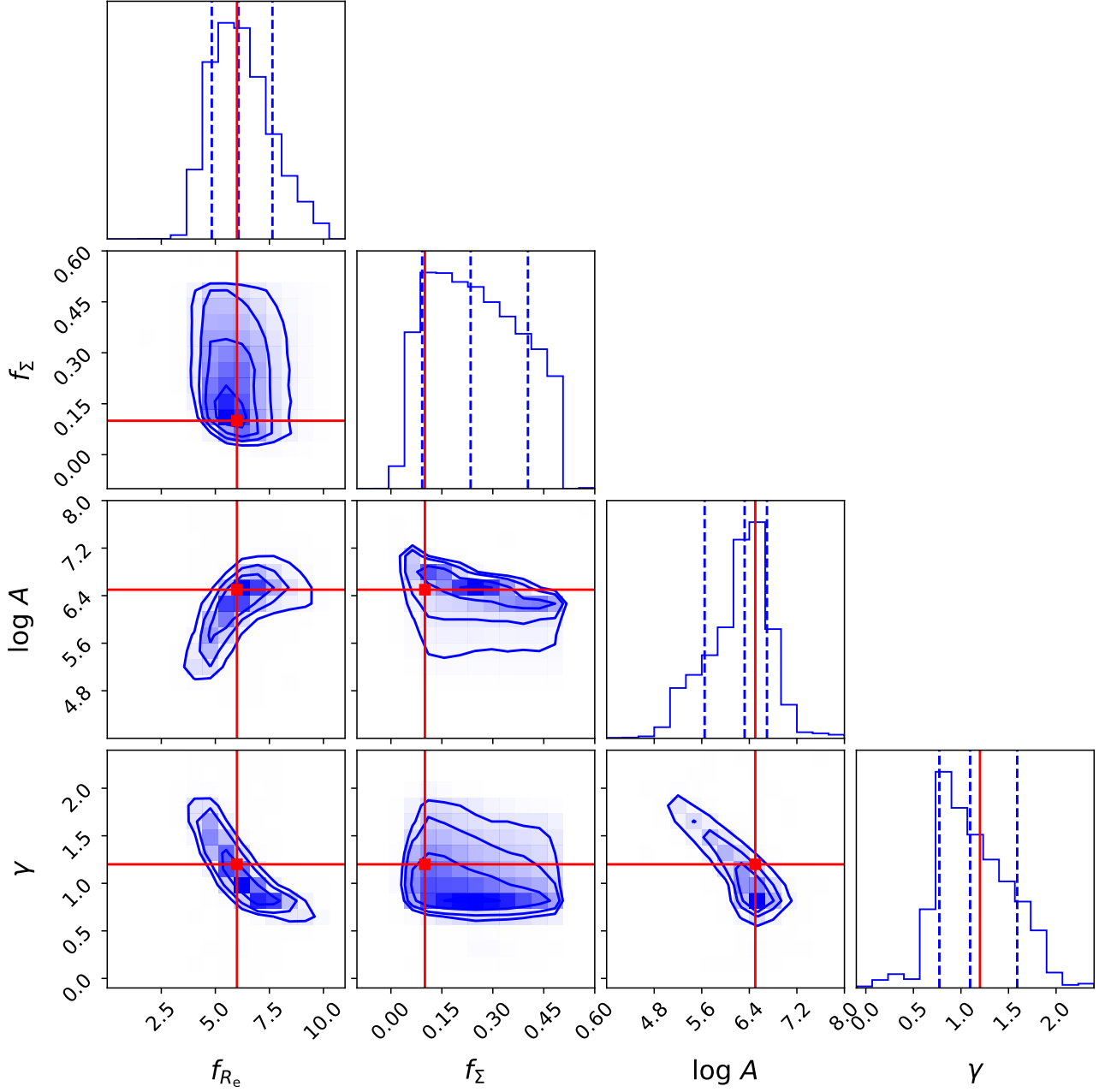


**Figure 8.** The forecast of confidence levels of the  $L_{\text{CII,SFR}} - \text{SFR}$  relation and [C II] halo parameters obtained by the optimized survey. We mark the input parameters by the crosses of vertical and horizontal lines.

Fudamoto Y., et al., 2022, arXiv e-prints, [p. arXiv:2206.01886](https://arxiv.org/abs/2206.01886)  
 Fudamoto Y., et al., 2023, arXiv e-prints, [p. arXiv:2303.07513](https://arxiv.org/abs/2303.07513)  
 Fujimoto S., et al., 2019, *ApJ*, **887**, 107  
 Fujimoto S., et al., 2020, *ApJ*, **900**, 1  
 Ginolfi M., et al., 2020, *A&A*, **633**, A90  
 Gong Y., Cooray A., Silva M., Santos M. G., Bock J., Bradford C. M., Zemcov M., 2012, *ApJ*, **745**, 49  
 Gong Y., Cooray A., Silva M. B., Zemcov M., Feng C., Santos M. G., Dore O., Chen X., 2017, *ApJ*, **835**, 273  
 Goodman J., Weare J., 2010, *Communications in Applied Mathematics and Computational Science*, **5**, 65  
 Harris C. R., et al., 2020, *Nature*, **585**, 357  
 Herrera-Camus R., et al., 2015, *ApJ*, **800**, 1  
 Herrera-Camus R., et al., 2021, *A&A*, **649**, A31

Hodge J. A., da Cunha E., 2020, *Royal Society Open Science*, **7**, 200556  
 Hollenbach D. J., Tielens A. G. G. M., 1999, *Reviews of Modern Physics*, **71**, 173  
 Hunter J. D., 2007, *Computing in Science & Engineering*, **9**, 90  
 Karkare K. S., Moradinezhad Dizgah A., Keating G. K., Breyse P., Chung D. T., 2022, arXiv e-prints, [p. arXiv:2203.07258](https://arxiv.org/abs/2203.07258)  
 Kennicutt Robert C. J., 1998, *ARA&A*, **36**, 189  
 Knudsen K. K., Richard J., Kneib J.-P., Jauzac M., Clément B., Drouart G., Egami E., Lindroos L., 2016, *MNRAS*, **462**, L6  
 Koprowski M. P., et al., 2018, *MNRAS*, **479**, 4355  
 Kovetz E. D., et al., 2017, arXiv e-prints, [p. arXiv:1709.09066](https://arxiv.org/abs/1709.09066)  
 Kovetz E., et al., 2019, *BAAS*, **51**, 101  
 Lagache G., Cousin M., Chatzikos M., 2018, *A&A*, **609**, A130  
 Lambert T. S., et al., 2022, arXiv e-prints, [p. arXiv:2210.10023](https://arxiv.org/abs/2210.10023)

- Le Fèvre O., et al., 2020, *A&A*, **643**, A1
- Leung T. K. D., Olsen K. P., Somerville R. S., Davé R., Greve T. R., Hayward C. C., Narayanan D., Popping G., 2020, *ApJ*, **905**, 102
- Li T. Y., Wechsler R. H., Devaraj K., Church S. E., 2016, *ApJ*, **817**, 169
- Madden S. C., et al., 2013, *PASP*, **125**, 600
- Mashian N., Sternberg A., Loeb A., 2015, *J. Cosmology Astropart. Phys.*, **2015**, 028
- Matthee J., Sobral D., Gronke M., Pezzulli G., Cantalupo S., Röttgering H., Darvish B., Santos S., 2020, *MNRAS*, **492**, 1778
- Mazure A., Capelato H. V., 2002, *A&A*, **383**, 384
- Mitra S., Choudhury T. R., Ferrara A., 2015, *MNRAS*, **454**, L76
- Olsen K. P., Greve T. R., Narayanan D., Thompson R., Toft S., Brinch C., 2015, *ApJ*, **814**, 76
- Olsen K., Greve T. R., Narayanan D., Thompson R., Davé R., Niebla Rios L., Stawinski S., 2017, *ApJ*, **846**, 105
- Pentericci L., et al., 2016, *ApJ*, **829**, L11
- Pizzati E., Ferrara A., Pallottini A., Gallerani S., Vallini L., Decataldo D., Fujimoto S., 2020, *MNRAS*, **495**, 160
- Pizzati E., Ferrara A., Pallottini A., Sommovigo L., Kohandel M., Carniani S., 2023, *MNRAS*, **519**, 4608
- Planck Collaboration et al., 2016, *A&A*, **594**, A13
- Prugniel P., Simien F., 1997, *A&A*, **321**, 111
- Pullen A. R., Doré O., Bock J., 2014, *ApJ*, **786**, 111
- Robertson B. E., Ellis R. S., Furlanetto S. R., Dunlop J. S., 2015, *ApJ*, **802**, L19
- Salvaterra R., Maio U., Ciardi B., Campisi M. A., 2013, *MNRAS*, **429**, 2718
- Schaan E., White M., 2021, *J. Cosmology Astropart. Phys.*, **2021**, 067
- Schaerer D., et al., 2020, *A&A*, **643**, A3
- Schechter P., 1976, *ApJ*, **203**, 297
- Serra P., Doré O., Lagache G., 2016, *ApJ*, **833**, 153
- Sérsic J. L., 1963, Boletín de la Asociación Argentina de Astronomía La Plata Argentina, **6**, 41
- Sersic J. L., 1968, Atlas de Galaxias Australes
- Sheth R. K., Tormen G., 1999, *MNRAS*, **308**, 119
- Sheth R. K., Mo H. J., Tormen G., 2001, *MNRAS*, **323**, 1
- Shibuya T., Ouchi M., Harikane Y., 2015, *ApJS*, **219**, 15
- Silva M., Santos M. G., Cooray A., Gong Y., 2015, *ApJ*, **806**, 209
- Silva B. M., Zaroubi S., Kooistra R., Cooray A., 2018, *MNRAS*, **475**, 1587
- Stacey G. J., Geis N., Genzel R., Lugten J. B., Poglitsch A., Sternberg A., Townes C. H., 1991, *ApJ*, **373**, 423
- Uzgil B. D., Aguirre J. E., Bradford C. M., Lidz A., 2014, *ApJ*, **793**, 116
- Uzgil B. D., et al., 2019, *ApJ*, **887**, 37
- Uzgil B. D., et al., 2021, *ApJ*, **912**, 67
- Vallini L., Gallerani S., Ferrara A., Pallottini A., Yue B., 2015, *ApJ*, **813**, 36
- Virtanen P., et al., 2020, *Nature Methods*, **17**, 261
- Vitral E., Mamon G. A., 2020, *A&A*, **635**, A20
- Wolfire M. G., McKee C. F., Hollenbach D., Tielens A. G. G. M., 2003, *ApJ*, **587**, 278
- Yue B., Ferrara A., 2019, *MNRAS*, **490**, 1928
- Yue B., Ferrara A., Pallottini A., Gallerani S., Vallini L., 2015, *MNRAS*, **450**, 3829

## APPENDIX A: PROFILE DEPROJECTION

The deprojection of the 2D surface density profile  $\Sigma(R)$  is the inversion of the Abel integral (Binney & Mamon 1982; Binney & Tremaine 1987)

$$\rho(r) = -\frac{1}{\pi} \int_r^{+\infty} \frac{d\Sigma}{dR} \frac{dR}{\sqrt{R^2 - r^2}}, \quad (\text{A1})$$

where  $r$  is the 3D radius,  $\rho(r)$  is the 3D density profile. For the Sérsic model of  $\Sigma(R)$ , the exact analytical expression of the above integral involves the Meijer G special function (Mazure & Capelato 2002; Baes & Gentile 2011) or Fox H function (Baes & Gentile 2011), both of them are complicated. Therefore, several analytical approximations are also proposed. They are described in detail in

Vitral & Mamon (2020) and references therein. Here we choose to use the analytical approximation given by Prugniel & Simien (1997). In this model, one writes the dimensionless 3D density profile as

$$\tilde{\rho}(x) = \frac{b_n^{(3-p_n)n}}{n\Gamma[(3-p_n)n]} x^{-p_n} \exp[-b_n x^{1/n}] \quad (\text{A2})$$

where  $x = r/R_e$ ,  $p_n$  is a function depending on the index  $n$ ,

$$p_n = 1 - \frac{0.594}{n} + \frac{0.055}{n^2}. \quad (\text{A3})$$

Therefore, in our model, the 3D luminosity density profile for the central galaxies can be written as

$$\begin{aligned} \rho_{\text{CII,g}}(r) &= \frac{L_{\text{CII,g}}}{4\pi R_{e,g}^3} \tilde{\rho}(x) \\ &= \frac{L_{\text{CII,SFR}}}{4\pi R_{e,g}^3} \frac{(b_n)^{(3-p_n)n}}{n\Gamma[(3-p_n)n]} x^{-p_n} \exp[-b_n x^{1/n}]. \end{aligned} \quad (\text{A4})$$

For the extended [C II] halo, since the exponential profile corresponds to the Sérsic model with  $n = 1$ , one can easily derive  $\rho_{\text{CII,h}}(r)$  by analogizing to Eq. (A4) and replacing  $L_{\text{CII,g}}$  with  $L_{\text{CII,h}}$ ,

$$\begin{aligned} \rho_{\text{CII,h}}(r) &= \frac{L_{\text{CII,h}}}{4\pi R_{e,h}^3} \frac{(b_1)^{(3-p_1)}}{\Gamma[(3-p_1)]} x^{-p_1} \exp[-b_1 x] \\ &= \frac{L_{\text{CII,SFR}}}{4\pi R_{e,g}^3} \frac{f_{\Sigma}}{f_{R_e}} \frac{1}{n} \frac{\Gamma(2)}{\Gamma(2n)} \frac{(b_1)^{2n} (b_1)^{(1-p_1)}}{\Gamma[(3-p_1)]} \\ &\quad \times x^{-p_1} \exp[-b_1 x]. \end{aligned} \quad (\text{A5})$$

This paper has been typeset from a  $\text{\LaTeX}$  file prepared by the author.